NASA CONTRACTOR REPORT

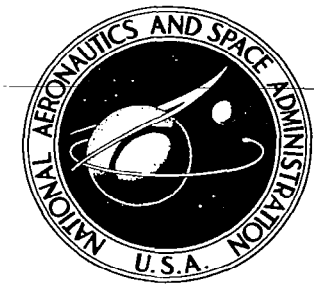

TIROS RADIATION MEASUREMENTS AND VARIATIONS IN ATMOSPHERIC HEATING

by Paul A. Davis

Prepared by
STANFORD RESEARCH INSTITUTE
Menlo Park, Calif.
for Goddard Space Flight Center

NATIONAL AERONAUTICS AND SPACE ADMINISTRATION • WASHINGTON, D. C. • OCTOBER 1966

NASA CR-581

TIROS RADIATION MEASUREMENTS AND VARIATIONS IN ATMOSPHERIC HEATING

By Paul A. Davis

Prepared under Contract No. NAS 5-9540 by
STANFORD RESEARCH INSTITUTE
Menlo Park, Calif.

for Goddard Space Flight Center

NATIONAL AERONAUTICS AND SPACE ADMINISTRATION

For sale by the Clearinghouse for Federal Scientific and Technical Information
Springfield, Virginia 22151 – Price $2.00

ABSTRACT

This study examines the implications of TIROS VII radiation measurements, especially in the infrared window region, to assessments of variations in diabatic heating or cooling of the atmosphere. With the aid of concurrent temperature, moisture, and cloud data, computations of the infrared cooling were performed for stations at a variety of locations in summer and winter. Correlations between the TIROS infrared window data and the computed infrared cooling are found to vary with height, latitude, and season. Although a positive correlation exists between the window data and the total infrared cooling for the entire depth of the atmosphere, especially on a large scale, it appears that the best correlation must exist for some cloud-bounded layer. Computations of the covariance betwen the infrared cooling and the total potential energy also display variations in space and time. Equivalent temperatures from the carbon dioxide channel on TIROS VII appear to be related to the total potential energy and cooling of the stratosphere.

Infrared window measurements and available solar reflectance measurements from limited samples are found to display a relationship to the relative water vapor and heat sources at the ocean surface. The sampling bias in albedo estimates based on solar reflectance measurements from TIROS was examined by generating typical scan-statistics on a computer and by using theoretical distributions of the reflected radiation from a turbid atmosphere. This degradation-free technique indicates that the anisotropy of the reflected radiation results in an underestimate of the global albedo.

From computational evidence, it is concluded that narrower, cleaner window measurements will be more useful than the broad-band window measurements of the past. In all phases of the work, it is apparent that cloud effects need further definition and study before the cloud data can be utilized effectively with radiation data.

CONTENTS

ILLUSTRATIONS

TABLES

ACKNOWLEDGMENTS

The author wishes to acknowledge the participation and assistance of personnel from the Aerophysics Laboratory. Especially noteworthy are the contributions from Robert L. Mancuso and William Viezee, both of whom coauthored earlier quarterly reports. Russell Trudeau, Melvin I. Smith, and James R. Moeller aided in the analyses of data. Mr. Moeller also introduced revisions of earlier computer programs.

I INTRODUCTION AND SUMMARY

The ultimate aim of studies of the type reported here is to render interpretations of satellite data in a manner suitable for eventual inclusion in numerical-dynamical models of the earth's atmosphere. Direct relationships of satellite measurements to atmospheric parameters are desired, preferably in linear form for ease in quantitative application. Major difficulties with the quantitative interpretation of existing satellite radiation data on any given scale include the anisotropy of emerging radiation, inhomogeneities or ambiguities in the viewed background, instrumental response degradation, and insufficient concurrent data for evaluation.

In an earlier study[1]* medium-resolution TIROS III radiation measurements were examined in conjunction with analyses based on concurrent meteorological observations for 4 X 4 degree grids over the United States in summer. Evidence suggested a general relationship between the distribution of Channel 2 (8-13.5 μ) temperatures and the distribution of the relative diabatic cooling within the atmosphere. The Channel 2 temperatures were correlated positively with the residual cooling from infrared cooling, solar heating, and the latent heat released by condensation; a negative correlation with the estimated surface heat flux to the atmosphere was indicated. In the daytime, Channel 3, covering the solar spectrum, provided useful data in combination with Channel 2. It was also demonstrated that the observed Channel 2 temperatures can be used to specify quantitatively the outgoing infrared flux from the earth/atmosphere.

---

* References are listed at the end of the report.

A primary objective of the present study was to extend the examination of satellite radiation measurements (in particular, Channel 2 of TIROS VII) and diabatic atmospheric variations to localities and times not considered in the earlier study, and to consider some vertical variation of the infrared cooling. In contrast to the earlier study, no attempt was made to analyze cloud and other meteorological observations over grid areas that were large relative to the sampled volume of atmosphere. Radiosonde data and coincident surface observations were accepted in unaltered form and satellite data were confined to an area, centered at the observing station, with a dimension equivalent to 1.25 degrees of longitude at the equator. All observations were restricted to 1200 GMT because of the maximum availability of conventional observations at this time. Since this restriction introduced a wide variety of local times and conditions, the infrared cooling was given computational emphasis in the analysis of the observed atmosphere. This limitation in scope was not intended to minimize the importance of the other diabatic components. In a relative sense the infrared cooling is usually not the most critical diabatic component, but laborious computations of the differential infrared cooling could be avoided if the Channel 2 response were sufficiently well correlated to the cooling. However, the correlation was not found to be persistent in space or time for the limited samples studied. Similarly, the suggested generation or destruction of potential energy varied in space and time. Other aspects of meridional and seasonal study are discussed in Sec. VI.

The reflected solar radiation is a vital part of the local radiation balance and provides an indication of the energy available for heating the lower boundary. An outstanding difficulty of the TIROS measurements has been the incompatibility of the quasiglobal albedo estimated from the solar reflectance channels and from Channel 2. Until the problem is resolved, the effectiveness of combining solar reflectance measurements with Channel 2 measurements is curtailed. Presumably, on-board calibration in future satellites will alleviate the difficulty by monitoring the degradation. Therefore, an examination was conducted of the bias in solar reflectance measurements, exclusive of degradation. It was

concluded that, because of the anisotropic nature of the emergent radiance, an underestimate of the large-scale albedo results from averaging of the typically restricted satellite samples. The most extreme underestimate was associated with a nonreflective lower boundary. Differences in the spectral distribution of incoming solar radiation and the emergent radiance from the atmosphere did not introduce significant spectral bias in the response of Channel 3 over a lower boundary with a low surface reflectance or over a surface with a high reflectance that was uniform throughout the visible and very near infrared spectrum.

For several selected winter and summer atmospheric soundings with ozone measurements, equivalent temperatures were computed for the spectral region of Channel 2, both with and without the ozone, and for a narrower and more transparent spectral region (10.5 to 11.1 μ). The computations for Channel 2 without ozone were related to those with ozone, so that credibility can be attached to patterns of Channel 2 temperature that are computed when the ozone distribution is unknown. The diurnal variation of temperature at the top of the ozone layer has negligible effect on the Channel 2 response. If measurements were obtained in the narrower, ozone-free window interval, it was determined that the equivalent temperatures would provide superior estimates of the temperature of a viewed surface with less limb darkening than Channel 2, and would still be a good estimator of the total outgoing infrared flux.

From a limited number of ship reports, observed Channel 2 temperatures were compared with estimates of the water vapor and heat transports to the atmosphere from the ocean. The winter sample suggested that the average transports varied as the average Channel 2 temperature, but the relationship was not well defined in summer. The estimated transports in summer appeared to relate better to the Channel 3 reflectance.

II SOLAR REFLECTANCE MEASUREMENTS FROM TIROS

If D is the measured effective radiant emittance, I_λ is the solar spectral irradiance at normal incidence at mean earth-sun distance, ζ is the solar zenith angle, n is a correction factor for deviations from the mean earth-sun distance, and f_λ is the effective spectral response of the radiometer, then the radiometric measurement can be interpreted as a reflectance from

$$r = D/n \cos \zeta \int I_\lambda f_\lambda d\lambda = D/S \cos \zeta \quad , \qquad (1)$$

where S is the effective solar flux at normal incidence.*

For a fixed optical system, differences in the spectral distributions of solar irradiance and reflected solar radiation can lead to a biased specification of the reflectance. In order to check the possible bias, the spectral distribution of the reflected radiation was postulated because the information for the top of an absorbing and scattering molecular-aerosol atmosphere was not available. For convenience, the postulation was based on two assumptions that were considered appropriate outside the regions of most intense absorption. For a given wavelength interval and solar zenith angle, the ratio of true reflected flux to the flux from a Rayleigh atmosphere was assumed to be a linear function of the ratio of the downward flux at the lower boundary to the downward flux at the bottom of the Rayleigh atmosphere. Furthermore, the later ratio was assumed to be proportional to the ratio of the direct fluxes at the specified angle. In application to a solar zenith angle of 53.1 degrees, it was concluded that differences in the spectral distributions of incident and reflected solar radiation produced negligible

---

* At mean earth-sun distance, S takes the values 494.3 W/m^2 and 108.5 W/m^2 for Channels 3 and 5, respectively, of TIROS VII.

bias in the reflectance measurements from Channel 3. This conclusion is valid only for an underlying surface with a low reflectance or for a surface with a high but spectrally uniform reflectance in the visible and very near infrared portion of the spectrum. Bias is also possible if measurements are made after the occurrence of pronounced spectrally dependent degradation.

Satellite measurements of the anisotropic reflected radiation have been restricted geometrically, i.e., low angles of solar incidence, large satellite nadir angles, and backward views close to the sun are excluded. The measured effective radiant emittance obtained from satellite data samples leads to biased estimates of the albedo when an isotropic distribution of emerging radiance is assumed. Both overestimates and underestimates occur, but the sampling procedure leads to a bias. An attempt was made to determine the bias in the planetary albedo that is deduced from averaged TIROS data under typical operating procedures.

Existing satellite radiation data have been affected both by the anisotropy of the emerging radiation and by the degradation in the radiometric response. The effect of one factor cannot be determined empirically without a proper joint account of the other factor. Variations of the degradation with intensity, wave number, and time are not well known because of the absence of suitable on-board calibration. A major difficulty in assessment is the possibility of a very rapid initial rate of degradation. In this study the problems of degradation were eliminated by generating data samples for a TIROS-type satellite on a computer.

The adopted orbital characteristics for the simulated TIROS included

(1) Height: 765 km
(2) Period: 100 minutes
(3) Orbital inclination: 63.5 degrees
(4) Orbital frequency: 14.4 orbits/day
(5) Nodal regression: 3 degrees/day (westward)

The right ascension of the spin vector was maintained at the right ascension of the sun and the declination of the spin vector was varied between ±35 degrees over a three-month period. Principal angles in the geometry of the emerging radiation from the sunlit hemisphere are illustrated in Fig. 1. Table I contains a list of definitions for the adopted symbols. Statistical summaries of data samples were described within discrete intervals of the angles ζ, β, and ϕ, but, in place of the relative azimuth ϕ, presentations were given in terms of the intermediate variable θ, the scattering angle. Here, the scattering angle is defined as zero in the forward direction.

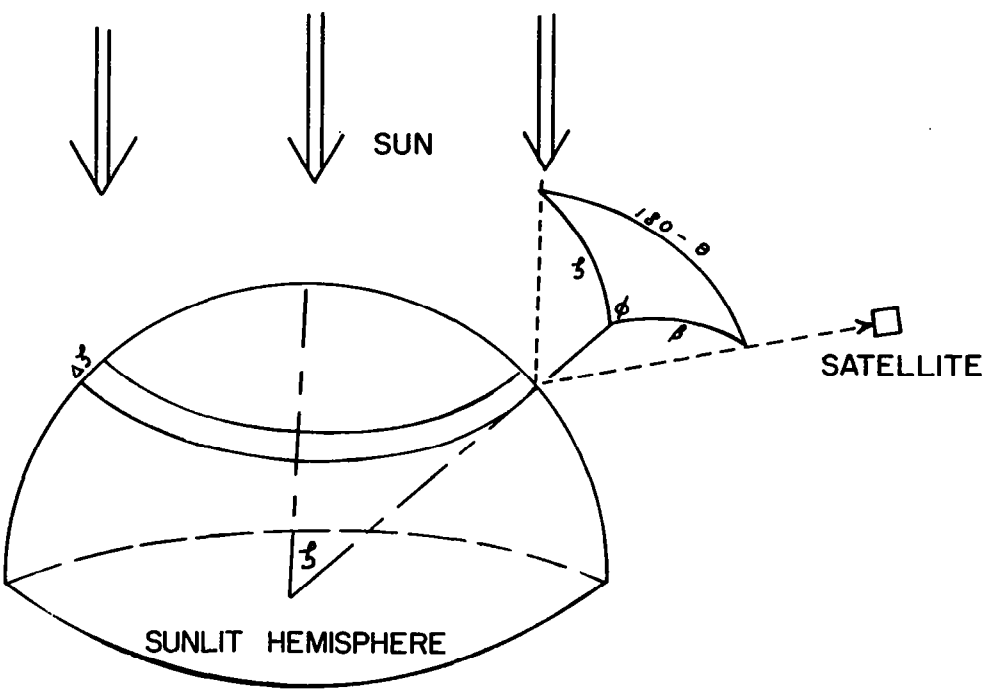

FIG. 1 GEOMETRY OF THE REFLECTED SOLAR RADIATION

Table I

DEFINITIONS OF SYMBOLS

Symbol	Definition
ζ	Solar zenith angle
β	Satellite zenith angle
α	Satellite nadir angle
ϕ	Relative azimuth angle
θ	Scattering angle ($\cos\theta = -\cos\zeta\cos\beta - \sin\zeta\sin\beta\cos\phi$)
F_s	Normal solar flux at top of atmosphere
$F_s/2$	Incident solar flux for hemisphere
I_r	Emergent radiance (function of ζ, β, and θ)
r	Radiant reflectance $\pi I_r/F_s \cos\zeta$
$\int \sin\zeta\, d\zeta$	Fractional area of zenith-angle strip around hemisphere
F_ζ	Emergent flux for a given solar zenith angle
F	Total emergent flux for sunlit hemisphere $= \int F_\zeta \sin\zeta\, d\zeta$
A	Total albedo for sunlit hemisphere

At solar zenith angle ζ, the emergent flux can be expressed as

$$F_\zeta = \int_0^{2\pi}\int_0^{\pi/2} I_r(\beta,\phi)\sin\beta\cos\beta\, d\beta\, d\phi$$

$$= \frac{2F_s\cos\zeta}{\pi}\int_0^{\pi}\int_0^{\pi/2} r\sin\beta\cos\beta\, d\beta\, d\phi \quad . \qquad (2)$$

In terms of the scattering angle, Eq. (2) can be written as

$$F_\zeta = \frac{2F_s\cos\zeta}{\pi}\int_0^{\pi/2}\left[\int_{\theta(\phi=0)}^{\theta(\phi=\pi)} r\,\gamma\, d\theta\right]\sin\beta\cos\beta\, d\beta \quad , \qquad (3)$$

where $\gamma = d\phi/d\theta$. The total albedo for the sunlit hemisphere becomes

$$A = 2F/F_s$$

$$= \frac{4}{\pi} \int_0^{\pi/2} \int_0^{\pi/2} \int_{\theta(\phi=\pi)}^{\theta(\phi=o)} r \gamma \, d\theta \sin \beta \cos \beta \, d\beta \sin \zeta \cos \zeta \, d\zeta \quad . \quad (4)$$

The total albedo for free viewing, i.e., viewing conducted in such a manner as to yield the true albedo, was approximated numerically by

$$A = \Sigma\Sigma\Sigma \, r \, k \, \Delta\theta \, \Delta\beta \, \Delta\zeta = \Sigma\Sigma\Sigma \, r \, w_o \quad , \quad (5)$$

where w_o is the weighting factor for the radiant reflectance in each increment and

$$k = \frac{\gamma \sin \beta \cos \beta \sin \zeta \cos \zeta}{\Sigma\Sigma\Sigma \, \gamma \sin \beta \cos \beta \sin \zeta \cos \zeta \, \Delta\theta \, \Delta\beta \, \Delta\zeta} \quad .$$

For the simulated satellite, the weighting factor w_o is no longer appropriate. Two sets of restrictions were imposed on the solar zenith angle and the radiometric nadir angle for views from a satellite with the given orbital characteristics:

(1) A maximum solar zenith angle of 80 degrees and a maximum radiometric nadir angle of 60 degrees, and

(2) A maximum solar zenith angle of 60 degrees and a maximum radiometric nadir angle of 40 degrees.

The weighting factors w_1 and w_2 were approximated for each array element as the ratio of the number of sample scan spots within the element to the total number of scanspots generated.

Radiometric data samples were generated over the sunlit hemisphere for the six months between minimum and maximum solar declination. Statistics encompassing the changing sun and satellite positions were based on computations for one orbit every four days without regard to specific geographical location. At 4-degree intervals along an orbit, scan-spot geometry was computed for every 4 degrees of satellite spin. Initially, the declinations of the spin vector and the sun were set at their minima and both right ascensions were located 90 degrees west of

the right ascension of the ascending node of the satellite orbit. During alternating-open-mode scans with overlapping data, only the scanlines with the smallest minimum radiometric nadir angle were included. Additional details of the geometrical computations and the computed weighting factors are given in Quarterly Progress Report 2.[2]

Figure 2 presents some of the information generated for each sampling procedure; the free-viewing distributions represent the optimum sampling frequencies. Ordinates represent the marginal sampling frequencies in percent per degree. The curve for a given angle does not reveal the joint frequencies of occurrence with other angles, but merely indicates the amount of time that a particular angle is encountered.

At large solar zenith angles, specular reflection and sun glint from water surfaces under clear skies add to the anisotropy of the emerging radiation. Furthermore, a backward enhancement of the reflected radiation can result from the illumination of an irregular cloud cover. In practice, some of the backward views would be eliminated as a result of solar contamination of the radiometric response. Although none of these factors has been included here, their frequency of occurrence in the sampling statistics can be inferred from the estimates summarized in Table II.

In addition to the scan statistics, an estimate of the sampling bias of reflectance measurements requires knowledge of the anisotropic distribution of the reflected solar radiation. The specification of r as a function of the three principal angles was accomplished by adaptation of the theoretical results of Feigelson, et al.,[4] and Atroshenko, et al.,[5] for their function VI and a 0.3 optical thickness. Computations of θ, interpolations, and some extrapolations were necessary in the adaptation. The surface reflectance was varied between zero and a number of isotropic reflectances. Since absorption was not included in the model, presentations for the simulated satellite data were restricted to albedo ratios, where the common denominator was the albedo obtained from free viewing. Albedo ratios are illustrated in Fig. 3.

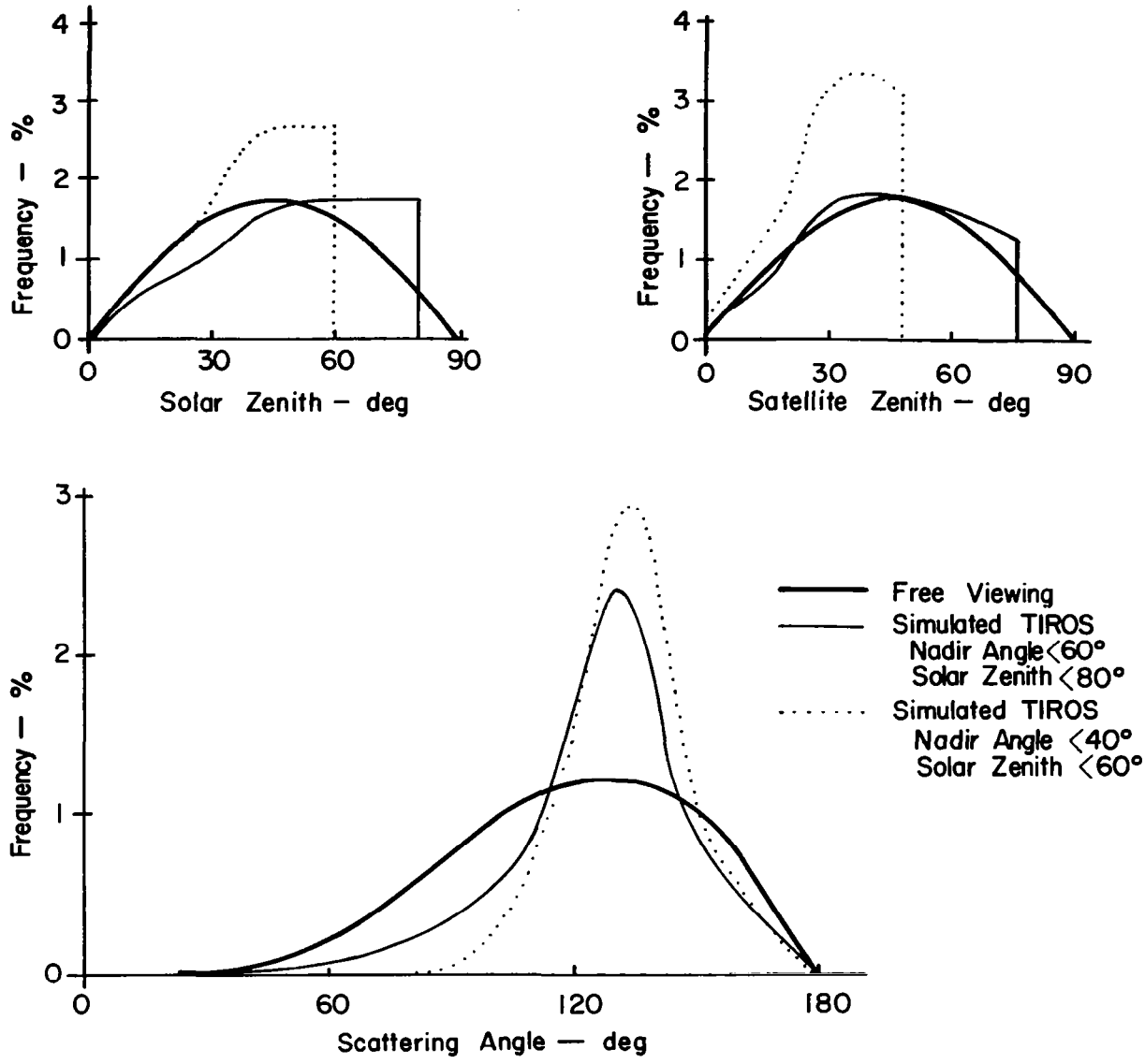

FIG. 2 MARGINAL FREQUENCY DISTRIBUTIONS OF VIEWS FOR SOLAR ZENITH ANGLE, SATELLITE ZENITH ANGLE, AND SCATTERING ANGLE

Table II

PERCENTAGE OF TOTAL VIEWS WITHIN 10 DEGREES OF BACKWARD AND SPECULAR DIRECTIONS FOR EACH SAMPLING DISTRIBUTION

		Solar Zenith Angle (degrees)									
		0-10	10-20	20-30	30-40	40-50	50-60	60-70	70-80	80-90	0-90
BACKWARD	I	0.09	0.25	0.36	0.41	0.36	0.28	0.17	0.07	0.01	2.00
	II	0.00	0.03	0.11	0.25	0.24	0.38	0.28	0.17	-	1.46
	III	0.00	0.08	0.31	0.46	0.24	0.00	-	-	-	1.09
SPECULAR	I	0.09	0.25	0.36	0.41	0.36	0.28	0.17	0.07	0.01	2.00
	II	0.00	0.04	0.25	0.14	0.02	0.10	0.09	0.05	-	0.69
	III	0.00	0.10	0.68	0.40	0.05	0.00	-	-	-	1.23

I: Free Viewing

II: Simulated TIROS ($\alpha < 60^{o}$, $\zeta < 80^{o}$)

III: Simulated TIROS ($\alpha < 40^{o}$, $\zeta < 60^{o}$)

BACKWARD: $\theta > 170^{o}$

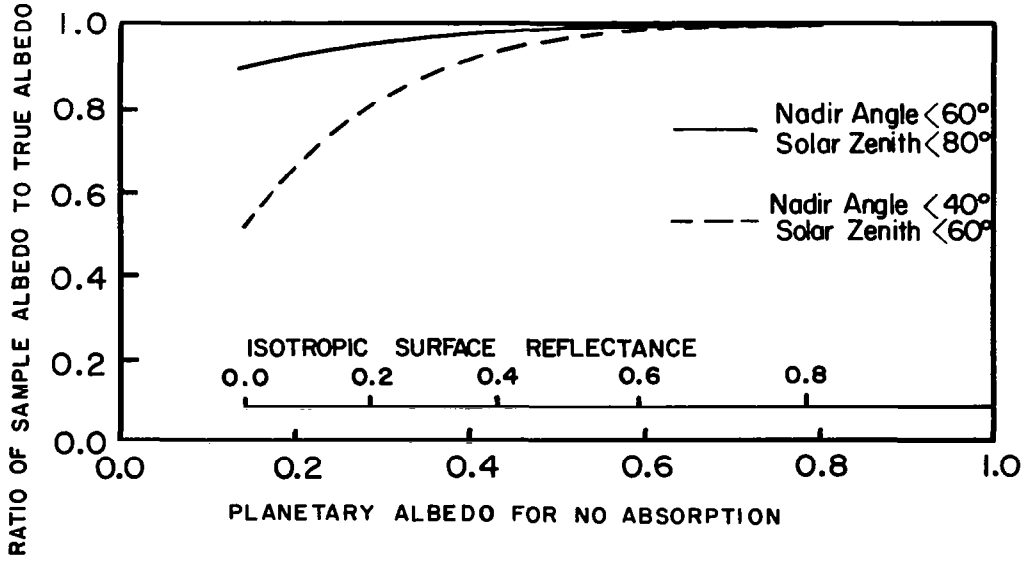

FIG. 3 RATIO OF SIMULATED TIROS ALBEDO TO THE TRUE ALBEDO

Figure 3 indicates that if the satellite samples were limited to a maximum ζ of 60 degrees and a maximum α of 40 degrees, a simple averaging of measurements over a nonreflecting lower boundary would lead to an estimate of the planetary albedo that would be only 51 percent of the true albedo. Of course, the nonreflecting lower boundary is associated with the smallest planetary albedo. This sizable bias could be maintained over a reflecting lower boundary only if the surface reflectance was anisotropic. As Fig. 3 shows, an increasing isoptropic surface reflectance will result in a decreasing underestimate of albedo because of the dominance of a reflective surface in the field of emerging radiation. Since cloud surfaces are not isotropic scatterers, it is not proper to associate a cloud reflectance with an isotropic surface reflectance, but it can be anticipated that the bias over a cloud surface exceeds the bias over an isotropic surface with the same albedo. As a first approximation, it was estimated from data presented by Feigelson, et al.,[6] that, with a planetary albedo of 50 percent, the ratio of the sample albedo to the true albedo over a cloud surface might be as low as 0.8 for the most restricted of the two simulated data sets.

III COMPUTATIONAL STUDY OF CHANNEL 2

Computer programs that were developed previously[3] for the infrared flux computations were revised to allow greater input flexibility and generality. Both the nontransparent and the semitransparent cloud models were combined into a single model that handles all previous applications. In addition, a black-body upper boundary can now be inserted above the semitransparent layer and a lower reference level, but this application would be uncommon. Equations and symbols are reviewed in the Appendix. The present model offers a practical tool, especially when combined with experimental data, for examining the effects of atmospheric structure or clouds, including nearly transparent cirrus, as a function of wavelength.

The absorption and emission of ozone was not included in the original model because the vertical distribution of ozone is seldom available. By neglecting the effect of ozone in computations of the variations in the Channel 2 temperature, it is assumed implicitly that variations in ozone are linked with variations in water vapor, i.e., larger ozone amounts with dryer air than with moist air. Recent radiosonde measurements of the vertical distribution of ozone made it possible to compute the Channel 2 temperature with and without the ozone and to compare the results.

With the limitation that the ozone amount M, reduced to standard conditions, is less than 1 atmos-cm along the path, the ozone transmission for the entire 9.6-μ band and the weak 9.0-μ band was approximated by

$$\tau = \exp\left\{-2.6M(1 - M)\left[1 + M(1 - M)^2/P\right]^{-1/2}\right\} , \qquad (6)$$

where P is the ratio of the effective pressure along the path to standard pressure. The constant factor probably should be a pressure-dependent parameter with a functional form governed by the definition of the effective pressure. In this application, the mean pressure was deliberately

used instead of an effective pressure. The formulation of Eq. (6) was based on the data of Walshaw,[7] but was applied to a slightly wider bandwidth in order to include the 9.0-μ band. On the basis of a presentation by Elsasser,[8] the band limits were set at 975 and 1125 cm^{-1}, a range over which the background absorption by water vapor is nearly uniform. In application, Eq. (6) was used for the flux transmission after replacing M by 1.66 M and it was assumed that joint flux transmission through atmospheric water vapor and ozone could be expressed by the product of the individual flux transmissions.

Using actual ozonesonde data[9] and cloudiness based on surface observations and the moisture profile, emittances were computed over the spectral region of Channel 2 (750 cm^{-1} to 1250 cm^{-1}) for stations at tropical, temperate, and polar latitudes for summer and winter. Results for clear skies and for the existing cloudiness are listed in Table III in terms of equivalent black-body temperatures for downward views from the 10-mb level at local zenith angles of 0 and 60 degrees. In addition to the entire spectral interval, results for the narrower, ozone-free interval between 900 and 950 cm^{-1} (10.5 to 11.1 μ) are included also. For all computations the lower boundary was assumed to be a black-body surface, and aerosol effects were not considered.

Figure 4 illustrates, for directly-downward views over existing cloudiness, the computed Channel 2 temperature (ozone included) and the reduction in temperature from the temperatures computed in the absence of ozone. The total cloudiness at each station is indicated in plotted form. With one exception, the computed temperature reduction due to ozone appears to be proportional to the Channel 2 temperature. In an independent study based on 106 radiosonde records, Wark, et al.,[10] computed the ozone effect by introducing modeled distributions of ozone, rather than actual ozone distributions. The dashed line in Fig. 4 represents the relationship derived from the presentation of Wark, et al.; the agreement is remarkable. These results suggest that computations of the outgoing infrared flux without the inclusion of ozone lead to realistic patterns, but that gradients in the patterns tend to be slightly

Table III

COMPUTED EQUIVALENT TEMPERATURES (°K) FOR DOWNWARD VIEWS FROM 10 mb
(Surface temperature and total ozone in atm-cm indicated below each station name)

Location	27 February 1963					
	Clear Sky			Existing Sky Cover		
	T_2^*	T_2	T_o	T_2^*	T_2	T_o
Canal Zone (298.8, .272)						
Air Mass 1:	293.3	289.0	294.8	266.7	263.7	267.1
Air Mass 2:	291.3	285.5	293.3	265.6	261.6	266.4
Fort Collins (279.5, .390)						
Air Mass 1:	278.2	273.7	279.0	267.5	263.7	268.0
Air Mass 2:	277.4	272.6	278.6	267.0	262.9	267.8
Fort Churchill (245.2, .450)						
Air Mass 1:	245.0	243.1	245.25	245.0	243.1	245.25
Air Mass 2:	245.0	243.2	245.29	245.0	243.2	245.29
Location	**14 August 1963**					
	Clear Sky			Existing Sky Cover		
	T_2^*	T_2	T_o	T_2^*	T_2	T_o
Canal Zone (299.2, .245)						
Air Mass 1:	293.0	289.2	295.1	267.0	264.4	267.7
Air Mass 2:	289.5	284.3	292.1	265.5	262.0	266.6
Albuquerque (291.5, .270)						
Air Mass 1:	288.5	284.7	289.8	286.5	282.9	287.8
Air Mass 2:	286.6	281.5	288.5	284.9	279.9	286.6
Fort Churchill (281.3, .330)						
Air Mass 1:	280.9	276.4	280.8	276.8	273.4	277.5
Air Mass 2:	279.3	274.7	280.5	276.2	271.8	277.2

T_2^*: 750-1250 cm^{-1}, without ozone

T_2 : 750-1250 cm^{-1}, ozone included

T_o : 900-950 cm^{-1}

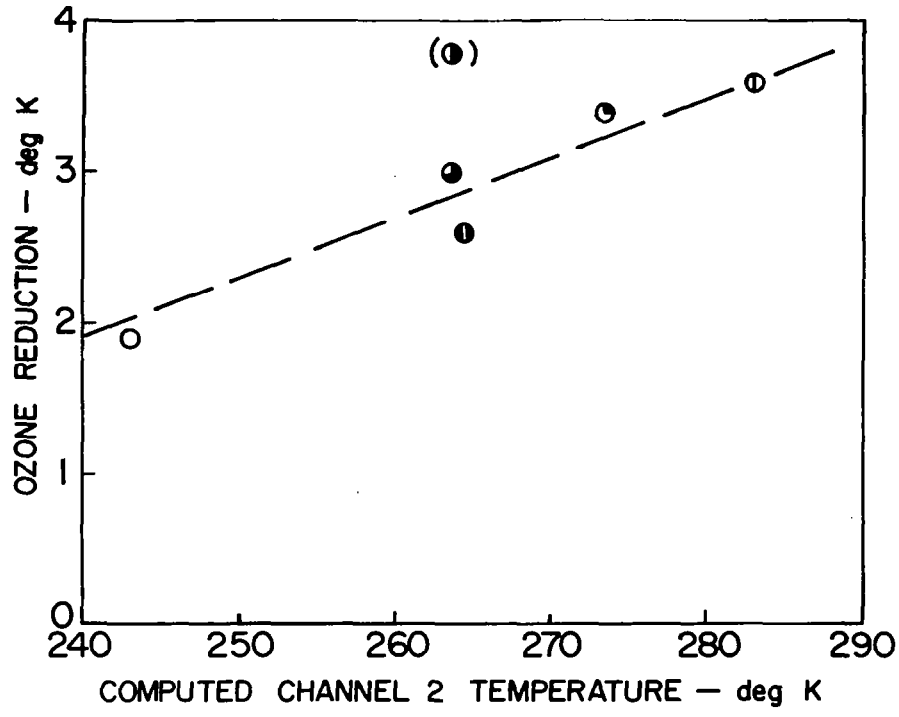

FIG. 4 COMPUTED CHANNEL 2 TEMPERATURE FOR DIRECTLY-DOWNWARD VIEWS AND CORRESPONDING TEMPERATURE REDUCTION DUE TO OZONE

exaggerated. Additional computations also revealed that sizable diurnal temperature changes near the top of the ozone layer have no significant diurnal effect (does not exceed $0.1^{\circ}K$) on the Channel 2 temperatures.

From Table III it is apparent that limb darkening of the narrower spectral interval is less than that of Channel 2. From the clear-sky computations it is also apparent that 900-950 cm^{-1} interval yields temperatures much closer to actual surface temperatures than does Channel 2. At Fort Churchill on 27 February 1963, a pronounced temperature inversion prevailed in the lower troposphere under clear skies. Here the computed equivalent temperature even exceeded the surface temperature slightly as a result of atmospheric contributions. Figure 5 illustrates the relationship between equivalent temperatures for both the broad and narrow spectral intervals and the corresponding total outgoing infrared flux. Linear least-square lines of fit are indicated on the diagram. It is apparent that the narrower window interval is about as good a descriptor of the variations in the total outgoing flux as is Channel 2.

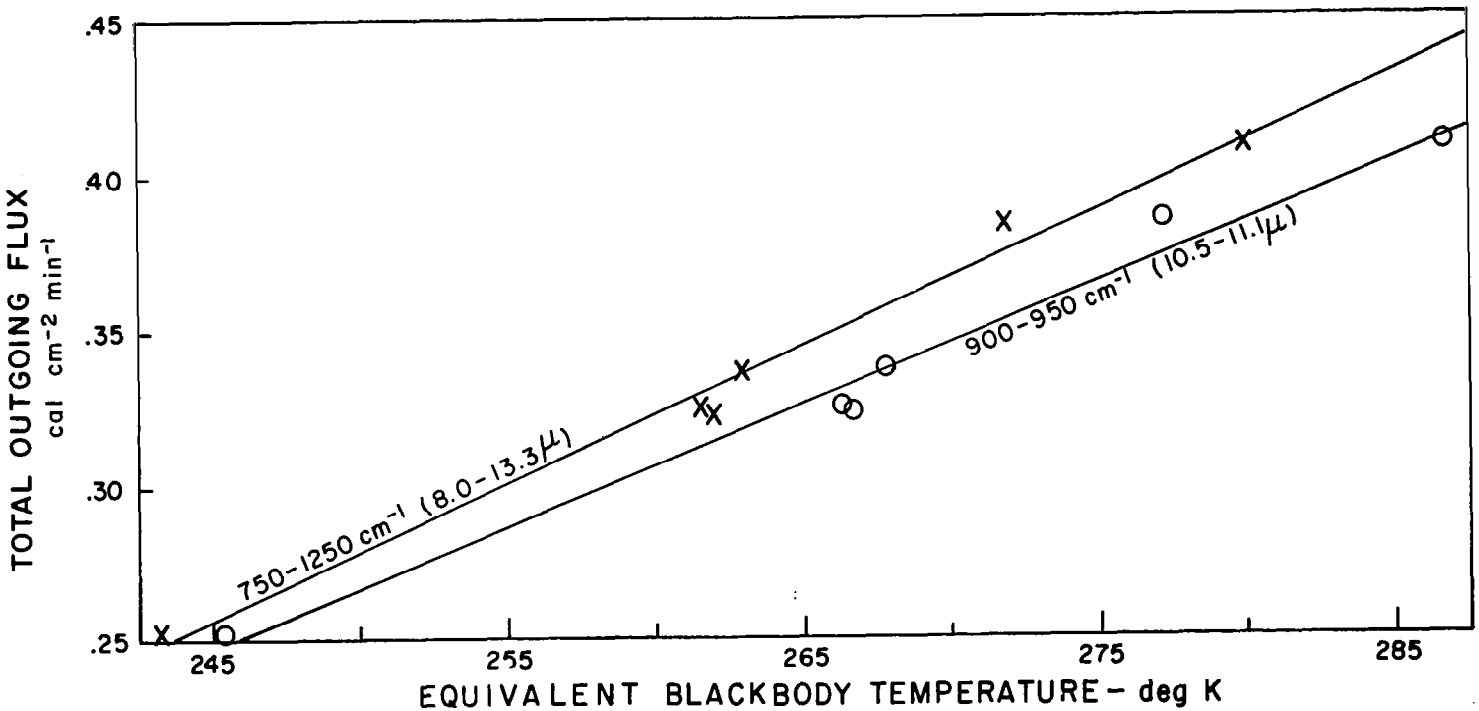

FIG. 5 EQUIVALENT BLACKBODY TEMPERATURES THROUGH AIR MASS 2 IN THE INTERVALS 8.0–13.3μ AND 10.5–11.1μ AND TOTAL OUTGOING INFRARED FLUX FOR SELECTED LOCALITIES

IV CHANNEL 2 MEASUREMENTS AND OCEANIC OBSERVATIONS

The climatological distribution of Channel 2 data (in terms of outgoing long-wave radiation) from TIROS VII are available for one year from Bandeen, et al.,[11] as a function of latitude. Since most of satellite data come from oceanic regions, where conventional data are difficult to obtain, it would be beneficial to place more emphasis on information about the air/sea interaction. Even the old climatological estimates[12] of evaporation minus precipitation and surface salinity over the oceans display a distribution similar to that of the averaged Channel 2 data, as can be seen in Fig. 6. The evaporation minus the precipitation expresses the input or extraction of water vapor to the atmosphere, a parameter of

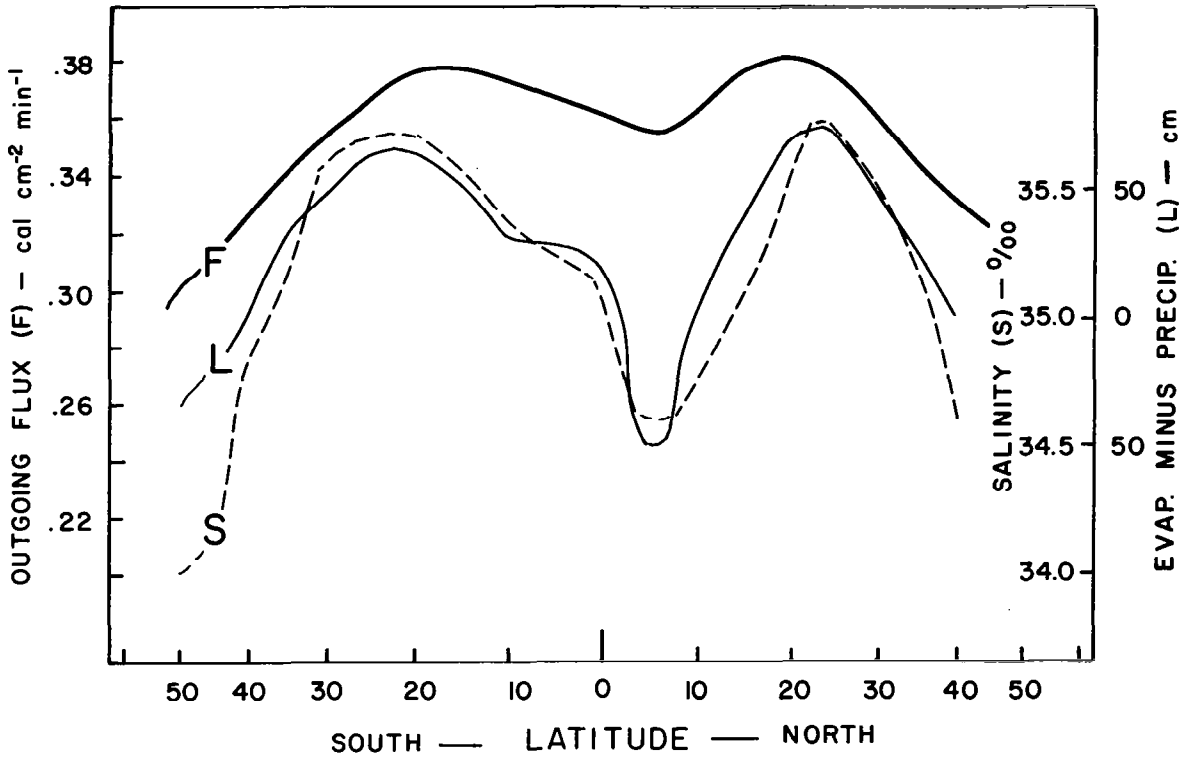

FIG. 6 ANNUAL MERIDIONAL DISTRIBUTION OF OUTGOING FLUX (F) FROM CHANNEL 2 OF TIROS VII AND OLD ESTIMATES OF EVAPORATION MINUS PRECIPITATION (L) AND SURFACE SALINITY (S) OVER THE OCEANS

direct applicability to numerical models of the atmosphere. Therefore, a preliminary examination was made of the possibility of using the satellite radiometric data to assess the distribution of water vapor and heat sources at the ocean surface.

Fortunately, the sparse oceanic observations from ship reports are not critically dependent on differences in local solar time between points at observation time. They do provide useful wind data and estimates of the vertical gradients of temperature and water vapor near the ocean surface (i.e., via measurements of the sea-surface temperature and the temperature and dew point of the air). If the data were available on a smaller scale and if the appropriate turbulent exchange coefficients were known, then it would be possible to describe the heat and water vapor transports at the surface. It was assumed here that the relative transports of heat and water vapor could be estimated from comparisons of the products of wind speed and air/sea temperature difference or air/sea vapor-pressure difference.

Ship reports were collected from oceanic regions for which mapped TIROS VII radiation data from Orbits 62 (June 1963) and 3284 (January 1964) were available. The data area for Orbit 62 crossed the Atlantic from polar to subtropical latitudes whereas data from Orbit 3284 were confined primarily to the Atlantic north of 47 degrees. In some instances it was likely that the conditions existing at the time of satellite passage differed from those in the 1200 GMT ship report. Some missing dew points were estimated from spatial analyses. Because of the limited sample sizes, the radiation data were ranked in three categories of approximately equal size. Average wind speeds, average temperature and vapor pressure differences, and average products were obtained in each category. Results are summarized in Table IV. The average products of wind speeds and estimated vapor-pressure or temperature gradients were subject to considerable uncertainty largely because of the sensitivity of the products to small errors at high wind speeds.

Table IV

SUMMARY OF AVERAGED DATA FROM SHIP REPORTS IN CATEGORIES OF RADIATION MEASUREMENTS FROM TIROS VII

(a) Channel 2 Categories, Orbit 62

T_2	R_3	V	Δe	ΔT	$V\Delta e$	$V\Delta T$
≥ 272	19.0	12.4	4.43	-0.63	56.7	-4.3
261-271	29.5	16.5	2.50	-0.51	28.8	-9.3
≤ 260	37.5	17.8	3.67	-0.42	65.3	-4.5

(b) Channel 3 Categories, Orbit 62

R_3	T_2	V	Δe	ΔT	$V\Delta e$	$V\Delta T$
≤ 20	272.9	11.8	6.46	-0.70	71.2	- 6.3
21-39	266.1	16.2	2.76	-0.61	49.4	- 2.1
≥ 40	260.1	18.8	1.32	-0.55	25.0	-11.4

(c) Channel 2 Categories, Orbit 3284

T_2	N	V	Δe	ΔT	$V\Delta e$	$V\Delta t$
≥ 259	.62	19.6	5.99	1.77	83.9	42.9
246-258	.85	14.3	2.39	1.54	34.7	22.7
≤ 245	.92	23.0	1.61	0.69	36.6	15.3

T_2 = Channel 2 temperature (degrees K)

R_3 = Channel 3 reflectance (percent)

V = wind speed (knots)

Δe = sea-air vapor pressure difference (mb)

ΔT = sea-air temperature difference (degrees K)

N = reported total cloud cover (tenths)

In Table IV(a), arranged according to Channel 2 temperatures, the average products V Δe and V ΔT show a nonlinear relationship to Channel 2, with minimum magnitudes in the intermediate temperature category. Originally it was anticipated that largest absolute magnitudes would occur with the highest Channel 2 temperatures, but, as a result of the lower wind speeds, this was not the case. Furthermore, a more linear relationship would be desirable for application. If, instead of the relative evaporation, it had been possible to consider "evaporation minus precipitation," the relationship could have been more nearly linear, but some shower activity did occur in regions with relatively high Channel 2 temperatures. The sea/air temperature differences for Orbit 62 showed that the average air temperature was warmer than the average water temperature for all categories. No distinct trend was apparent for the relative heat transports, partly because of wind speed-stability relationships.

Since Channel 3 reflectances were available for Orbit 62, the data were grouped and averaged in categories of the Channel 3 reflectance, as shown in Tablve IV(b). The most significant change from the summary in Table IV(a) is the improved categorical variation of the sea/air vapor-pressure difference and of the estimated relative evaporation. The relative evaporation is largest for the lowest Channel 3 reflectances even though the wind speed is lowest in this category.

No Channel 3 reflectances were available for the winter case, but the average reported total cloud cover is tabulated for each Channel 2 category in Table IV(c). All of the average sea/air temperature differences were positive, since the air was colder than the water. Now the estimated relative heat transport increased with increasing Channel 2 temperature, as did the vapor pressure and temperature differences. The estimated relative evaporation was a maximum for the highest Channel 2 temperature category and nearly the same for the other categories. In this case it is most likely that the quantity "evaporation minus precipitation" would have demonstrated a good positive correlation with the Channel 2 temperature.

V DATA SELECTION AND EVALUATION

Mapped radiation date from TIROS VII for selected orbits were examined for possible rectification errors and for distortions of features of interest. Orbits 62 and 3284, discussed above, provided good summer and winter data samples near the 1200 GMT radiosonde and surface observation time in conjunction with satellite photographs that contained distinct landmarks. Portions of the analyzed data are discussed below and have been discussed in more detail previously.[13]

Landmarks in Canada and Africa indicated that the rectification for Orbit 62 remained very good throughout the single open mode scans of the radiometer. Data from the solar reflectance channels agreed well with the cloudiness and yielded the same consistent patterns. Data from Orbit 61, which overlapped the Orbit 62 track over Canada about 100 minutes earlier, indicated that a significant warming of the Channel 2 temperatures had occurred over clear land areas by Orbit 62. Channel 2 patterns follow extensive areas of cloudiness quite well, but smaller cloud features can be lost or distorted in the Channel 2 patterns. Figure 7 illustrates a data sample over the Atlantic; numbered points provide references for comparison of patterns. The photograph reveals a marked cloud spiral, along with a distinct sun glint area on the sea surface. Mapped reflectance data from Channel 3 show less of the cloud organization, chiefly because of the poorer resolution of the radiometer. Due to differences in the viewing geometry and (possibly) to averaging of different scan spots, the sun glint did not appear in the Channel 3 map, but would have been difficult to distinguish from cloudiness without photographs if it had appeared. The Channel 2 map bears little resemblance to the photograph. Apparently the cloud tops were generally low; the area of the spiral is generally indicated by the 275°K isotherm. The lowest Channel 2 temperatures in Fig. 7 occur north of the spiral in an area of low reflectance (probably cold, tenuous cirrus). The synoptic analysis for the area of Fig. 7 merely indicated a weak, diffuse, quasistationary front.

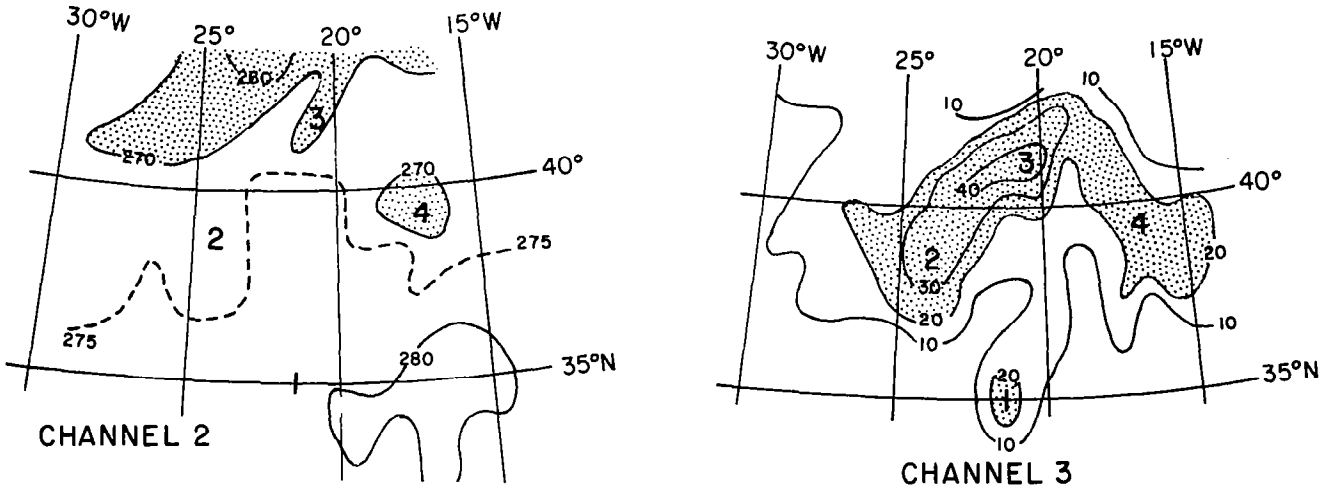

FIG. 7 ISOPLETHS OF CHANNEL 2 TEMPERATURE (°K) AND CHANNEL 3 REFLECTANCE (%) WITH SELECTED FRAME FROM CONCURRENT CLOUD PHOTOGRAPHS. (Orbit 62, TIROS VII, 23 June 1963)

Figure 8 presents some of the Channel 2 and vidicon data from Orbit 3284.

The lakes in the snow-covered region around Point 4 in Fig. 8 are too small for the resolution of Channel 2. Also, Channel 2 fails to show a contrast between land and the southeastern Black Sea (Point 5), but the photograph shows the Black Sea despite some thin cloudiness. The only pronounced synoptic aspect of the region (shown in the insert) is revealed by the Channel 2 temperature pattern.

As the southeastern portion of the illustrated strip was approached, the scanning mode was about to change from single open to alternating open mode. In this region the radiation map shows errors in rectification. The presence of coastal cloudiness suggested that the 280°K isotherm should be entirely offshore over the Arabian Sea. The cloudy region labeled 2 is shown in the photograph to cover the southern coastal region of the Gulf of Oman. Also in the photograph, the snow-covered mountainous region extends southeastward from Point 3. All of these features and the Persian Gulf indicate that the rectification of the radiation data after Point 3 was in error, with a resultant northeastward displacement from the true positions. Therefore, unless rectification corrections are made in order to avoid a mismatch with local conventional data, it appears desirable to avoid data very near or in the alternating open mode scan. If a data listing is used instead of a map, the change in scanning mode is easily spotted, bad scan lines can be omitted, and specific nadir angles can be selected.

Listings of the radiation data for portions of seven orbits were selected to provide comparisons with computations based on concurrent 1200 GMT surface and upper-air observations at a variety of latitudes and locations in summer and winter. The 1200 GMT observation was selected because of the abundance of published surface observations for the time throughout the Northern Hemisphere. Unfortunately, microfilm copies of original teletype records had to be searched for much of the 1200 GMT upper-air data outside of North America. Without both the surface and upper-air data at a station it is not possible to specify the cloudiness.

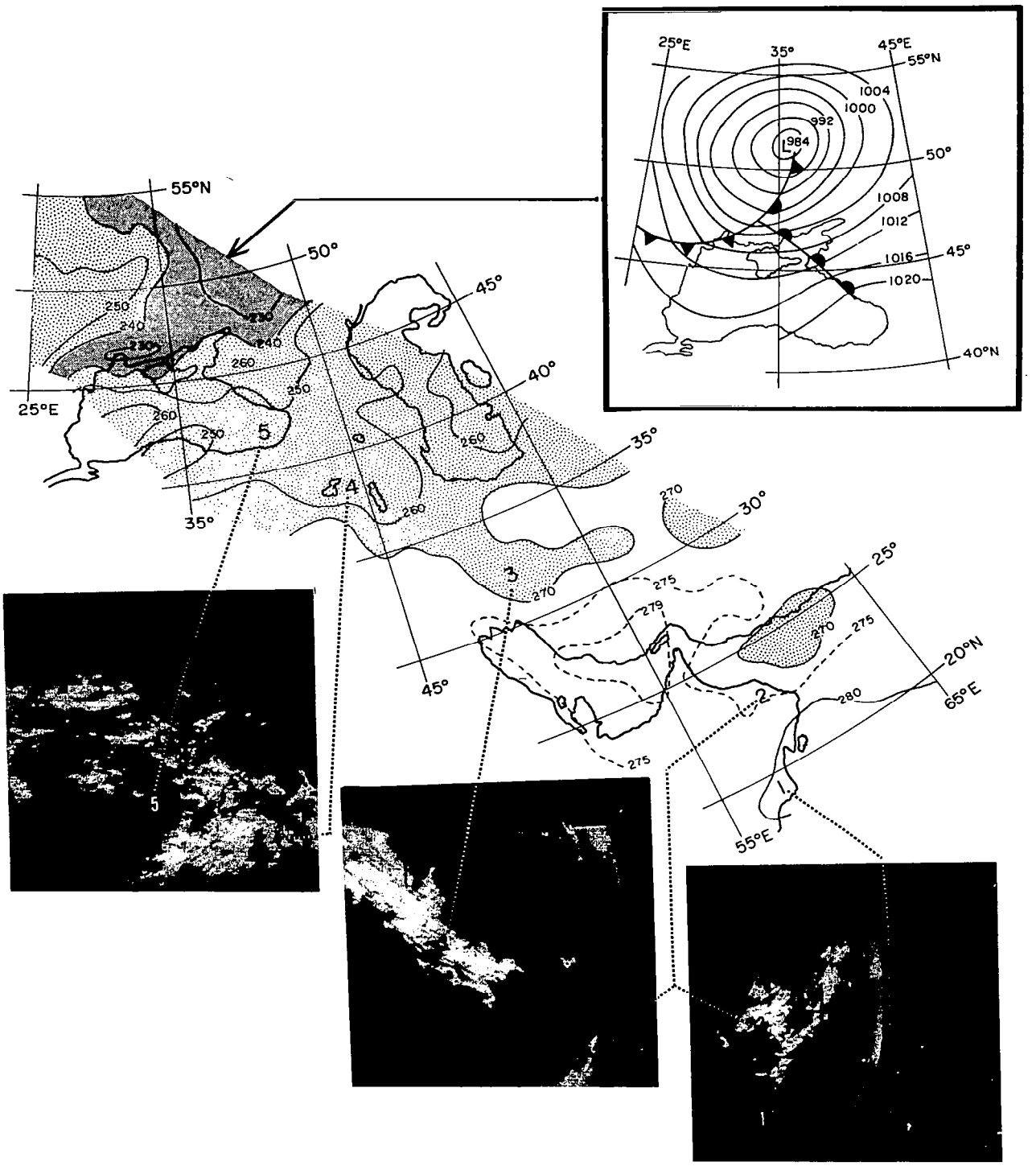

FIG. 8 ISOPLETHS OF CHANNEL 2 TEMPERATURE (°K) AND SELECTED FRAMES FROM CONCURRENT CLOUD PHOTOGRAPHS. (Orbit 3284, TIROS VII, 27 January 1964. Inset shows sea-level isobars (mb) and surface fronts in vicinity of Black Sea)

After considerable scrutiny, the final data sample was reduced to 50 radiosonde stations, 27 in June-July 1963 and 23 in December-January 1963/64. Many of the original soundings were discarded because of incomplete upper-air or surface data, transmission errors, repetition by nearby stations, or because of the inability to situate a cloud layer in the temperature-moisture structure. Other data were discarded on the basis of the radiometric data. For each accepted station it was required that three or more radiometric scan spots with nadir angles less than 51 degrees fall within a 75 X -75-nmi square centered at the station. With only a few exceptions, most radiometric nadir angles were less than 46 degrees. Of the three or more acceptable scan spots that were averaged at each station, it was also required that the nadir angles be sufficiently close to maintain a limb darkening smaller than the estimated relative accuracy ($2^{o}K$) of Channel 2. For angles larger than 33.5 degrees, the limb-darkening restriction was estimated by expressing the minimum allowable nadir angle as a linear function of the logarithm of the maximum nadir angle: $\alpha_{MIN} = 236 \log \alpha_{MAX} - 360$. Finally, some data had to be discarded because of obvious discrepancies between the observed boundary conditions and the satellite view. In particular, several coastal soundings had to be discarded because adjacent warm waters visible to the satellite were not represented in the conventional data. Sometimes a rapid change in the local cloud cover also occurs in a short interval between observation time and satellite passage.

Due to the shortage of tropical stations, several African radiosonde records for 0600 GMT were added. For these stations the lower portions of the soundings were modified to accommodate the 1200 GMT surface reports.

Prior to performing infrared computations with the data, all cloud heights and amounts had to be specified and the temperatures and specific humidities had to be extended to the "top" of the modeled atmosphere. In summer the top was set at 0.1 mb and in winter at 0.06 mb. All observed temperature profiles were extrapolated (if necessary) to 10 mb with the aid of some observations; above the 10-mb level the temperatures (based on Murgatroyd)[14] listed in Table V were introduced. All specific

humidities were extrapolated to the 100-mb level. Above 100 mb, the specific humidities were assigned the values listed in Table V. Above 10 mb a constant specific humidity of 0.06 g/kg was assumed.

Table V

MODELED UPPER-LEVEL TEMPERATURE AND MOISTURE

SPECIFIC HUMIDITY (g/kg)

Pressure (mb)	Latitude (deg N)			Pressure (mb)	Latitude 5-65
	5-35	35-50	50-65		
100	0.0040	0.0050	0.0060	40	0.013
90	0.0043	0.0052	0.0062	35	0.016
80	0.0050	0.0057	0.0066	30	0.020
70	0.0061	0.0064	0.0072	25	0.025
65	0.0067	0.0068	0.0076	20	0.034
60	0.0076	0.0076	0.0081	15	0.049
50	0.0096	0.0096	0.0096	10	0.060

TEMPERATURE (deg K)

Pressure (mb)	Latitude (deg N)			
	5-20	20-35	35-50	50-65
	Summer			
1.0	280	280	287	293
0.1	240	233	227	230
	Winter			
0.7	280	273	261	246
0.2	257	257	260	261
0.06	225	225	230	242

Cloud boundaries were introduced on the basis of surface observations and the temperature-moisture profiles. In some cases the middle cloud locations were difficult to specify, but the high-cloud specifications are excessively difficult. In this study, all high clouds were treated as a single level. Since reliable moisture information is seldom available in the upper troposphere, high-cloud locations were frequently based on a subjective examination of the temperature structure. All of the cirrus were arbitrarily assigned a transmittance, ranging between 0.1 and 0.6, depending on the apparent degree of saturation. During the infrared computations, results for each viewed cloud were weighted by the fraction of the view covered by the cloud.

Computations of the total potential energy between two levels, p_i and p_j, were described by

$$E_T = p_i Z_i - p_j Z_j + \frac{c_p}{g} \int_{p_j}^{p_i} T \, dp \qquad (7)$$

where Z is the height of the pressure surface. Where necessary, the height of the 10-mb level was taken from the climatological value given by Murgatroyd.

VI CHANNEL 2 MEASUREMENTS AND INFRARED COOLING

Table VI lists the original arrangement of the 50 radiosonde stations and some of the analyzed and computed quantities. The actual profiles of pressure, temperature, and specific humidity are not reproduced here. The listed cloudiness, C, for each station represents the reported total cloud amount minus the product of the unobstructed cirrus (if any) and its assumed transmittance. For example, if the total cloud amount was 0.8 and half of the total was due to cirrus occurring with no lower clouds and with a transmittance of 0.5, then the listed cloudiness would be 0.6. The effective cloudiness is a cloud of amount C so situated as to yield the computed infrared flux when combined with clear skies of amount 1-C. Other items included in Table VI are defined in the List of Symbols. At all points the station height was taken as the lower boundary and the surface pressure was used instead of sea-level pressure. All water clouds and the lower boundary were assumed to be blackbodies in this study, even though the infrared model allows arbitrary emissivities.

In order to check the apparent relative degradation of the Channel 2 response for the selected data samples, eight stations from July 1963 and eight from January 1964 were examined because they included the observed range of Channel 2 temperature. Figure 9 shows a plot of the Channel 2 temperatures and the associated outgoing infrared flux at 10 mb computed for the existing cloud conditions. Good relationships between the observations and computations are apparent. An estimated line of fit fails to reveal any difference with respect to orbit. Therefore, no degradation corrections were applied to the seasonal data used in this study of relative magnitudes, even when both sets of data are combined. For studies requiring absolute measures or involving other data, degradation corrections probably are necessary.

Table VI

STATION SUMMARY AND PARTIAL LIST OF PARAMETERS

C:	Total cloud amount	Orbit 61:	23 June 1963
p_s:	Surface pressure (mb)	Orbit 135:	28 June 1963
T_2:	Channel 2 temperature (deg K)	Orbit 238:	5 July 1963
W_T:	Precipitable water in total column (pr-cm)	Orbit 356:	13 July 1963
E_T:	Total potential energy, surface-10 mb (kj/cm^2)	Orbit 2662:	16 December 1963
N_p:	Net upward IR flux at subscripted pressure (cal cm^{-2} min^{-1})	Orbit 3210:	22 January 1964
		Orbit 3284:	27 January 1964

Station	Orbit	C	p_s	T_2	W_T	E_T	N_{10}	N_{200}	N_{500}	N_{sfc}
5 - 20°N										
61-052	135	0.42	985	286.3	3.20	255.0	0.368	0.355	0.307	0.129
65-201	135	0.90	1008	259.9	5.34	259.6	0.326	0.308	0.159	0.048
65-578	135	0.86	1012	275.9	4.63	260.7	0.346	0.327	0.222	0.053
91-334	238	0.15	1011	286.0	5.01	261.7	0.410	0.392	0.291	0.102
20 - 35°N										
61-401	135	0.50	974	291.5	1.71	256.9	0.387	0.368	0.252	0.159
47-778	356	0.40	1004	279.3	4.33	262.8	0.420	0.399	0.302	0.082
47-827	356	0.40	981	280.9	5.09	257.4	0.406	0.383	0.286	0.077
47-909	356	0.00	980	284.0	3.65	256.8	0.407	0.383	0.281	0.141
72-259	356	0.94	994	266.9	4.06	259.0	0.336	0.315	0.214	0.056
35 - 50°N										
08-221	61	0.00	946	285.1	1.79	237.4	0.442	0.419	0.346	0.196
08-302	61	0.30	1013	277.4	3.85	263.3	0.390	0.363	0.270	0.128
72-451	356	1.00	924	260.2	3.49	243.7	0.325	0.304	0.171	0.000
72-456	356	1.00	978	238.7	5.10	255.1	0.253	0.227	0.081	0.026
72-469	356	0.34	840	275.2	1.39	224.6	0.348	0.326	0.263	0.125
72-576	356	0.00	834	271.1	1.31	220.9	0.386	0.363	0.281	0.156
72-768	356	0.25	936	273.1	1.79	241.7	0.375	0.346	0.285	0.110
72-785	356	0.10	936	271.2	1.88	243.3	0.388	0.364	0.280	0.120
50 - 65°N										
Ship B	61	1.00	1013	264.2	0.96	255.6	0.335	0.325	0.258	0.009
04-270	61	0.00	1011	267.8	1.30	254.0	0.371	0.338	0.278	0.155
72-836	61	0.00	1020	274.8	1.15	262.5	0.408	0.385	0.318	0.152
72-848	61	0.46	985	263.7	3.83	255.9	0.360	0.336	0.209	0.072
72-906	61	0.87	1007	252.3	2.41	257.0	0.290	0.259	0.149	0.051
70-231	356	1.00	1003	251.0	2.05	255.1	0.285	0.246	0.181	0.051
70-273	356	0.60	1012	266.3	2.81	257.7	0.361	0.332	0.259	0.054
70-326	356	0.10	1016	273.9	2.00	257.8	0.378	0.347	0.296	0.094
72-879	356	0.25	937	273.1	1.74	242.1	0.363	0.337	0.242	0.111
72-964	356	0.80	932	253.3	1.83	239.1	0.307	0.276	0.194	0.056

Table VI (Concluded)

Station	Orbit	C	p_s	T_2	W_T	E_T	N_{10}	N_{200}	N_{500}	N_{sfc}
5 - 20°N										
78-501	3210	0.25	1014	280.7	2.95	261.2	0.422	0.405	0.320	0.110
78-526	3210	0.10	1016	280.7	2.52	260.6	0.414	0.400	0.316	0.122
78-866	3210	0.10	1014	282.4	2.70	260.7	0.419	0.404	0.318	0.136
78-897	3210	0.40	1015	280.7	3.01	261.4	0.404	0.388	0.306	0.076
20 - 35°N										
47-744	2662	0.60	1018	265.4	1.02	253.1	0.344	0.325	0.262	0.070
72-206	3210	0.49	1021	269.3	1.59	258.0	0.363	0.345	0.258	0.070
72-208	3210	0.35	1019	267.4	0.94	256.7	0.315	0.287	0.235	0.128
72-211	3210	0.47	1020	265.7	2.15	259.3	0.359	0.340	0.247	0.077
35 - 50°N										
47-401	2662	0.85	1011	261.4	0.53	243.3	0.295	0.261	0.215	0.038
47-412	2662	1.00	1011	251.0	0.99	245.7	0.286	0.250	0.201	0.026
47-420	2662	0.90	1010	248.6	0.49	243.6	0.285	0.255	0.206	0.026
33-345	3284	0.50	972	254.3	0.57	231.7	0.294	0.274	0.229	0.095
33-815	3284	1.00	994	235.1	0.80	240.6	0.263	0.242	0.135	0.035
72-600	3284	0.25	1009	258.8	0.80	245.1	0.334	0.319	0.274	0.121
72-811	3284	0.94	992	238.7	0.31	235.6	0.244	0.221	0.172	0.043
50 - 65°N										
Ship B	3284	0.75	995	258.1	0.76	241.1	0.324	0.305	0.259	0.053
03-026	3284	1.00	1008	231.3	1.24	243.4	0.248	0.229	0.114	0.018
10-184	3284	0.14	1025	260.1	0.59	246.0	0.316	0.301	0.253	0.155
26-781	3284	0.18	973	234.0	0.18	227.1	0.261	0.240	0.209	0.126
26-850	3284	0.06	977	244.6	0.22	229.2	0.286	0.264	0.242	0.146
33-008	3284	1.00	992	251.1	0.50	234.2	0.270	0.249	0.210	0.012
34-009	3284	1.00	956	235.4	0.49	225.3	0.237	0.215	0.175	0.000
72-816	3284	0.60	992	246.2	0.60	237.7	0.257	0.233	0.150	0.054

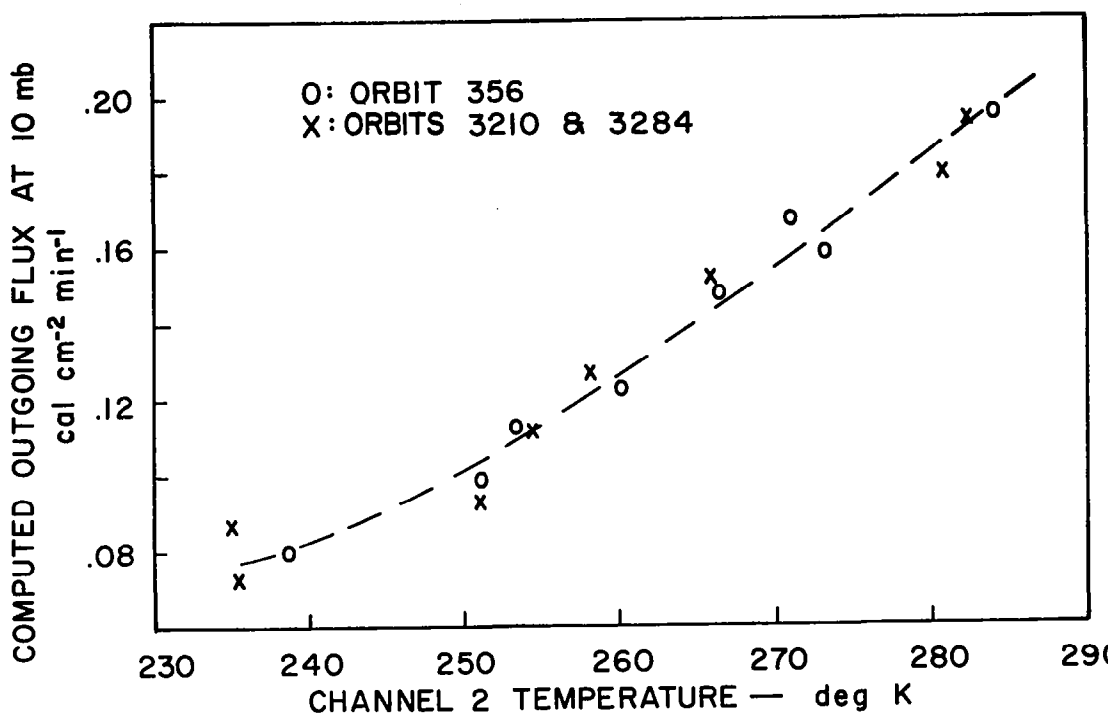

FIG. 9 COMPUTED OUTGOING INFRARED FLUX FOR THE SPECTRAL INTERVAL 750–1250 cm^{-1} AT 10 mb AND OBSERVED CHANNEL 2 TEMPERATURES FROM TIROS VII OVER SELECTED LOCALITIES

A check on the significance of the latitudinal arrangement of stations is afforded by selected graphs for summer and winter in Fig. 10. It is apparent that the Channel 2 temperature (which is correlated with the net upward flux of infrared radiation) displays a meridional variation that could be anticipated from a larger data sample. The meridional variation of the infrared cooling computed from the limited data also appears reasonable and shows a large-scale relationship to the Channel 2 temperature. The relationship between the Channel 2 temperature and the total potential energy between the surface and 10 mb is weak in the summer, partly because of terrain effects on E, but improves in the winter. The cloudiness appears to be related to the mean E in the summer, but not in the winter. Furthermore, the relationship between the Channel 2 temperature and the total infrared cooling rate (R) is more pronounced in the winter than in the summer because of stronger meridional gradients in the winter.

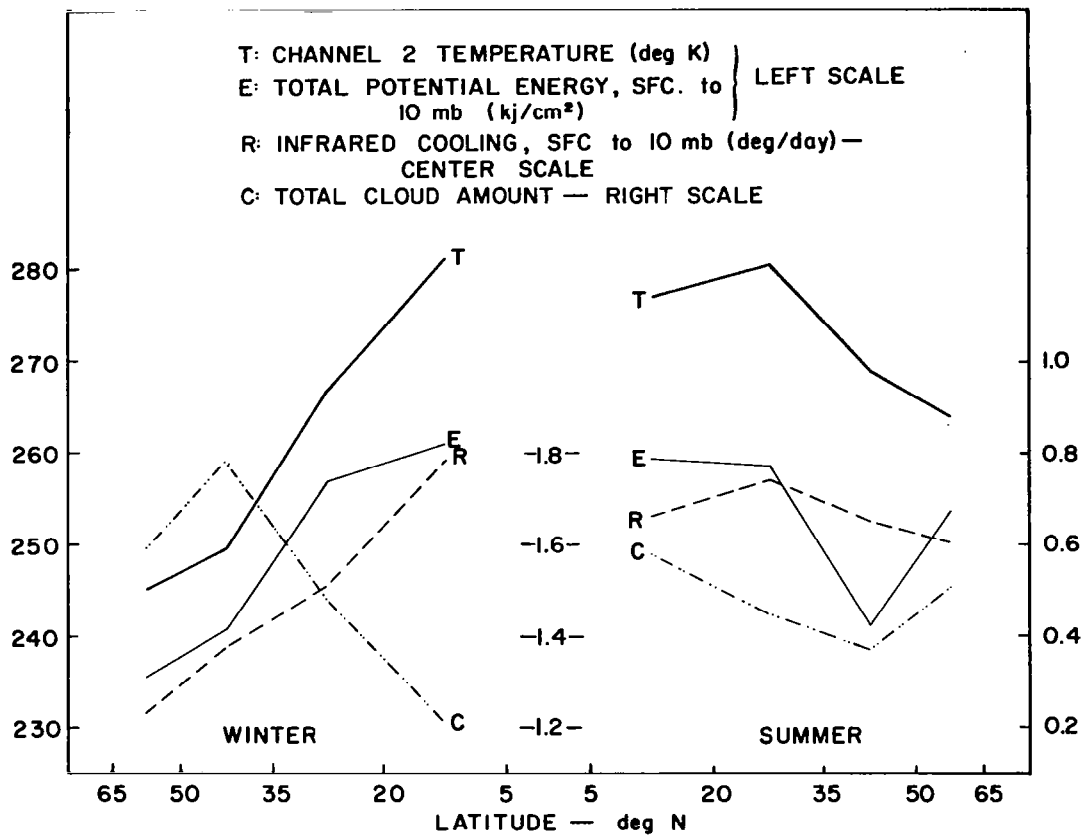

FIG. 10 SAMPLE DISTRIBUTION OF AVERAGE CHANNEL 2 TEMPERATURE, TOTAL CLOUD AMOUNT, INFRARED COOLING (surface to 10 mb), AND TOTAL POTENTIAL ENERGY (surface to 10 mb)

Data from Channel 1, covering the 14.8 to 15.5-μ region of carbon dioxide absorption, often appear to be noisy unless a number of observations are averaged. Since only relative averages were examined during each of two periods, degradation correction factors were not applied initially. However, analyses[15] of the apparent degradation have indicated different corrections for floor and wall measurements, so that even relative distributions may be distorted when data samples contain an unequal number of floor and wall measurements. Consequently, the latest available recommendations[15] for correction were applied. For

the given data sample it appeared that an increased (reduced) correction for low (high) temperatures through the floor side would have resulted in a more acceptable corrected distribution, but no basis for such a modification was established.

Since the total potential energy represents a temperature average, it was anticipated that E for the uppermost layer, 200 to 10 mb, should be related to the Channel 1 temperature measurements. Figure 11 shows that Channel 1 data, at least during the summer, can provide a general measure of the total potential energy for the atmospheric layer. A gross relationship is also displayed between the Channel 1 data and computed infrared cooling rates for water vapor and carbon dioxide in the layer. Since the total potential energies above 200 mb over the tropics were of the same magnitude in both seasons, Fig. 11 indicates that

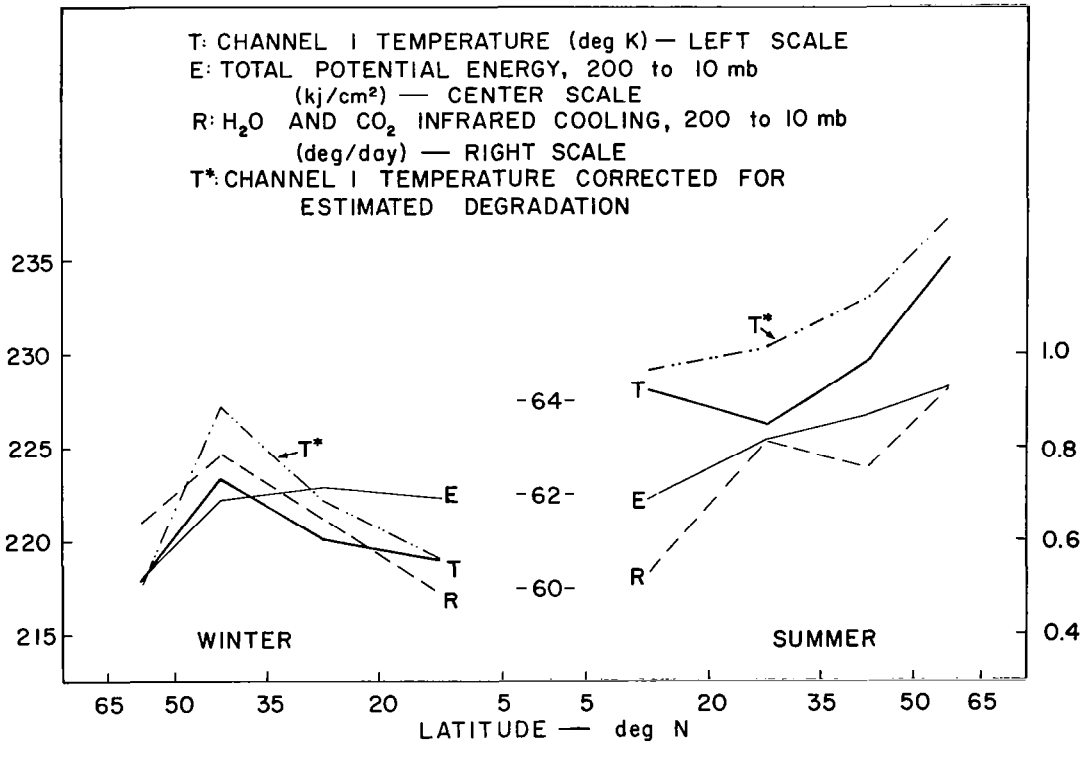

FIG. 11 SAMPLE DISTRIBUTION OF AVERAGE CHANNEL 1 TEMPERATURE, INFRARED COOLING WITHOUT OZONE (200 mb to 10 mb), AND TOTAL POTENTIAL ENERGY (200 mb to 10 mb)

significant degradation of Channel 1 did occur between July 1963 and January 1964. The average temperature above 200 mb was subject to more uncertainty in winter than in summer because of extrapolations of observed data, but the possibility of inadequate corrections for degradation exists also. Average nadir angles associated with the Channel 1 temperatures in Fig. 11 did not vary significantly; no limb brightening corrections were included. Variations in the temperature structure and the associated brightening means that all variations in the Channel 1 temperature need not correspond to temperature changes of a fixed mass layer.

Since the most useful relationship between satellite data and other data would be linear, linear correlation coefficients were computed for most of the analyzed variables. An abbreviated summary of correlation coefficients, means, and standard deviations is presented in Table VII. The small samples south of 35^{o}N were not included as separate categories in Table VII. In the latitude zone 35^{o}N to 65^{o}N the correlation between the Channel 2 temperature and the total atmospheric infrared cooling is small both in summer and winter. When seasonal and meridional contrasts are minimized, the Channel 2 temperature is correlated better with the infrared cooling of the lower troposphere than of the entire atmosphere. The correlation coefficients for the upper troposphere also are larger but reversed in sign. When more southerly latitudes are included the correlation in winter increases in a positive sense along with the disappearance of the reversal in altitude, probably because of the low amounts of cloudiness equatorward in the winter data sample. As the scale is increased by joining data from all latitudes and seasons, the climatic factors of seasonal and meridional change in mean temperatures and cooling rates are apparent, with a resultant improvement in the positive correlation between Channel 2 and the infrared cooling for the entire atmospheric column. Such a relationship may be of use only for large-scale or long-term studies. In general, the correlation between Channel 2 and the infrared cooling was not found to be persistent in space and time, even though Channel 2 is always well correlated with the outgoing infrared flux. In the winter data sample, if the outgoing fluxes (and associated surface temperatures) are excluded, T_2 is correlated best with the total

Table VII

SELECTED LINEAR CORRELATION COEFFICIENTS

C: Total cloud amount

T_2: Channel 2 equivalent temperature (deg K)

R_T: IR cooling rate, surface-10 mb (deg/day)

R_L: IR cooling rate, surface-500 mb (deg/day)

R_U: IR cooling rate, 500 mb-200 mb (deg/day)

W_L: Precipitable water, surface-500 mb (pr-cm)

W_U: Precipitable water, 500 mb-200 mb (pr-cm)

	C	T_2	R_T	R_L	R_U	W_L	W_U		Mean	Std Dev
Summer (35 - 65°N)										
								C	0.45	0.387
T_2	-0.82							T_2	266.2	11.15
R_T	0.25	0.15						R_T	1.63	0.21
R_L	-0.17	0.54	(0.77)					R_L	1.93	0.51
R_U	0.47	-0.55	0.11	-0.51				R_U	1.67	0.52
W_L	0.41	-0.45	0.01	-0.50	0.79			W_L	2.13	1.01
W_U	0.52	-0.64	-0.14	-0.63	0.86	0.76		W_U	0.125	0.102
Winter (35 - 65°N)										
								C	0.68	0.348
T_2	-0.27							T_2	247.2	9.99
R_T	0.83	0.20						R_T	1.30	0.25
R_L	0.50	0.42	(0.81)					R_L	1.67	0.50
R_U	0.45	-0.42	0.22	-0.38				R_U	1.07	0.50
W_L	0.41	0.03	0.49	0.07	0.68			W_L	0.58	0.26
W_U	0.44	0.07	0.37	-0.10	0.63	0.59		W_U	0.028	0.016
Summer and Winter (35 - 65°N)										
								C	0.55	0.387
T_2	-0.62							T_2	257.6	14.23
R_T	0.24	0.49						R_T	1.48	0.28
R_L	0.03	0.52	(0.76)					R_L	1.81	0.52
R_U	0.23	0.02	0.41	-0.26				R_U	1.40	0.60
W_L	0.04	0.29	0.46	-0.07	0.77			W_L	1.42	1.09
W_U	0.19	0.05	0.28	-0.26	0.78	0.83		W_U	0.081	0.090

	C	T_2	R_T	R_L	R_U	W_L	W_U		Mean	Std Dev
Summer (5 - 65°N)										
								C	0.47	0.365
T_2	-0.65							T_2	270.5	12.20
R_T	0.16	0.13						R_T	1.65	0.21
R_L	-0.20	0.39	(0.76)					R_L	1.93	0.50
R_U	0.44	-0.31	0.14	-0.50				R_U	1.78	0.53
W_L	0.31	-0.02	0.30	-0.14	0.63			W_L	2.72	1.32
W_U	0.41	-0.27	0.04	-0.50	0.86	0.71		W_U	0.157	0.105
Winter (5 -65°N)										
								C	0.56	0.338
T_2	-0.56							T_2	256.6	15.68
R_T	0.20	0.60						R_T	1.42	0.30
R_L	0.14	0.57	(0.87)					R_L	1.82	0.51
R_U	0.06	0.24	0.50	0.02				R_U	1.24	0.49
W_L	-0.39	0.78	0.73	0.52	0.64			W_L	1.08	0.85
W_U	-0.28	0.67	0.49	0.21	0.59	0.73		W_U	0.051	0.037
Summer and Winter (5 - 65°N)										
								C	0.51	0.356
T_2	-0.59							T_2	264.1	15.54
R_T	0.10	0.52						R_T	1.55	0.28
R_L	-0.07	0.48	(0.78)					R_L	1.88	0.51
R_U	0.19	0.18	0.45	-0.19				R_U	1.53	0.58
W_L	-0.02	0.48	0.58	0.14	0.72			W_L	1.96	1.39
W_U	0.13	0.24	0.34	-0.19	0.80	0.79		W_U	0.108	0.097

potential energy in the upper troposphere.

The effective cloud amount C, which is negatively correlated to T_2, does not appear to be an outstanding statistic by itself. Apparently, the cloud information can be used advantageously only in conjunction with other data. For example, cloud information could be used with temperature data to provide estimates of the distribution of precipitable water. The precipitable water, through its close average association with temperature, is well correlated to the total potential energy of the atmosphere (not given in Table VII). When no clouds are present, more specifically, if no high clouds are present, then Channel 2 measurements can be combined with measurements in the 6.3 μ band of water vapor to obtain estimates of the precipitate water in the upper troposphere (above 500 mb). From a computational viewpoint such estimates are feasible even in the absence of knowledge of the actual temperature structure at the time of measurement. One of the better correlation coefficients in Table VII is between the precipitable water for the layer 500 to 200 mb and the infrared cooling for the same layer.

An analysis of the correlations in Table VII is complicated by many factors, including nonlinear multivariate relationships, but a most restrictive factor is the lack of large samples of independent data. Nevertheless, the results are not unreasonable, even though variations in the temperature-moisture structure and in cloud type produce considerable scatter. Some of the difficulty of analysis in the presence of scatter is illustrated in Fig. 12 for the relationship between T_2 and the computed cooling in the upper and lower troposphere between $35^{o}N$ and $65^{o}N$. In both summer and winter the correlations are reversed for the two layers. The reversal is probably due to moisture and cloud effects, such that the lower Channel 2 temperatures over cloudy regions are associated with reduced cooling below the clouds and increased cooling just above the clouds. Apparently, if the Channel 2 temperature is to be related locally to the infrared cooling, particular layers exist for the optimum correlations. These layers would be cloud bounded during cloudy conditions. When data from winter and summer are combined

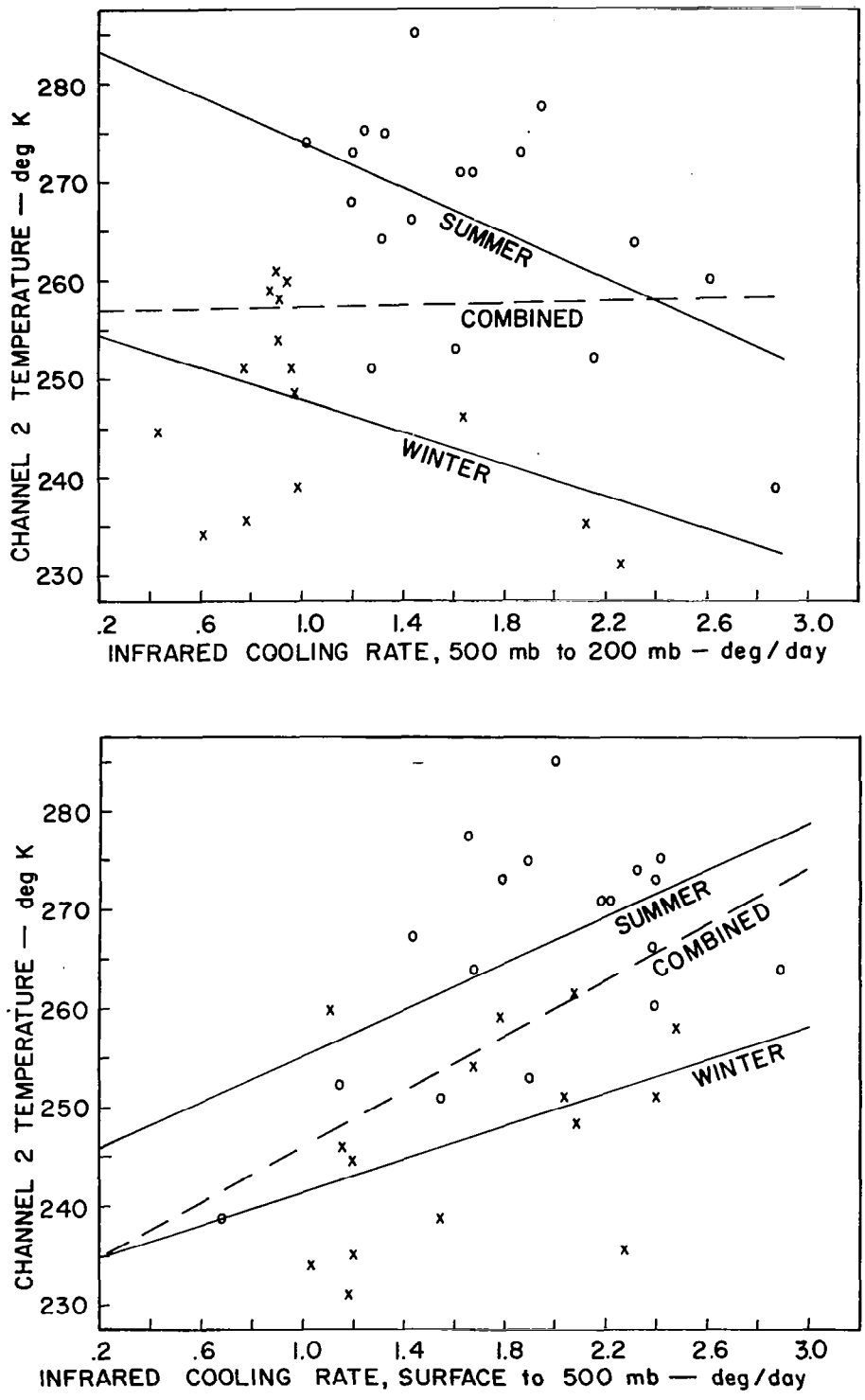

FIG. 12 CORRELATION AND REGRESSION BETWEEN CHANNEL 2 TEMPERATURE AND COMPUTED INFRARED COOLING RATES IN UPPER AND LOWER TROPOSPHERE FOR SELECTED DATA SAMPLES, 35° TO 65° N LATITUDE

in Fig. 12, the combined correlation increases in a positive sense because of the winter to summer increase of both T_2 and the cooling rates. In the lower troposphere this results in an enhanced correlation, but in the upper troposphere the original negative correlation in each season is merely eliminated.

Combination of summer and winter data from Channel 2 could have been hampered by response degradation, although evidence of this was not apparent. Another complicating factor with TIROS is the variation of local local solar time, especially over land stations without significant cloudiness. As has been shown earlier[3], the diurnal variation of the outgoing flux, to which Channel 2 responds, can be reversed from the diurnal variation of the total infrared cooling for the same basic atmospheric structure. This is so because the net upward radiation at the surface varies more than the outgoing flux at the top of the atmosphere. The situation could be remedied by a sunsynchronous satellite. Variations in surface emissivity also introduce variability in the Channel 2 response.

The covariance between infrared cooling and temperature provides an indication of the destruction of total potential energy by infrared processes, although other diabatic processes (solar absorption, the release of latent heat, and the surface heat flux) may predominate. Table VIII presents summaries of computed covariances between the infrared cooling in deg/day and the total potential energy in kj/cm^2 for several data groupings. Computations for the layer between 200 mb and 10 mb are not included because of uncertainties due to extrapolated temperature profiles and the neglect of ozone, but the entire layer between the surface and 10 mb is included for comparisons with the lower and upper troposphere. A positive covariance suggests infrared destruction of total potential energy, but does not distinguish betweeen zonal and eddy available potential energy. Thus, when the scale is expanded in latitude, the increased emphasis on variations in the zonal component may obscure results associated with the eddy component, with the least pronounced change during summer.

Results in Table VIII suggest that the infrared cooling acts to destroy total potential energy in the zone between $5^{o}N$ and $35^{o}N$ and in the upper troposphere. In the zone between $35^{o}N$ and $65^{o}N$ a generation of total potential energy of the lower troposphere is suggested, but is pronounced only in the summer. When the entire atmospheric column is considered, the tendency toward greater destruction is probably indicative of stratospheric destruction, but a net summertime generation persists in mid-latitudes. With the combination of all latitudes, the enhanced destruction in winter is associated with the large-scale destruction of zonal potential energy by infrared cooling.

Table VIII

COMPUTED COVARIANCES BETWEEN INFRARED COOLING RATE (deg/day) AND TOTAL POTENTIAL ENERGY (kj/cm^2)

	Surface -10mb	Surface -500 mb	500 mb -200 mb
Summer			
$5-35^{o}N$	.31	.22	.04
$35-65^{o}N$	-.34	-1.97	.42
$5-65^{o}N$	.06	-1.20	.46
Winter			
$5-35^{o}N$	.34	.20	.20
$35-65^{o}N$	.61	-.07	.25
$5-65^{o}N$	2.16	1.42	.86
Summer and Winter			
$5-35^{o}N$	.33	.30	.31
$35-65^{o}N$	.91	-.95	1.13
$5-65^{o}N$	1.40	.02	1.18

VII CONCLUDING REMARKS

The most specific information that can be obtained directly from satellite radiation measurements is the specification of the net incoming and outgoing radiation at the top of the atmosphere. With the aid of solar reflectance measurements, it is logical to obtain this information from measurements through an infrared window portion of the spectrum. There is evidence that the same radiometric equipment can provide useful information on the water vapor and heat sources at the ocean surface for all sky conditions.

It is difficult to specify the net infrared flux at the lower boundary, and therefore, the total infrared cooling, from Channel 2 measurements alone. Other satellite observational techniques and improved or expanded surface observations are needed. Except on a very large scale, there is no conclusive evidence that the total infrared cooling of entire atmospheric columns is of vital operational importance. The infrared cooling and other diabatic heat sources in particular layers may be of more interest and may be more easily inferred remotely.

It is apparent that the objective use of cloud information in conjunction with satellite radiation data is necessary. In this connection the effects of clouds, including thin cirrus, on remote measurements or inferences of the temperature profile, the moisture content, and the surface temperature must be studied. Improved radiosonde measurements of moisture at cirrus levels would aid considerably any evaluation analysis. Routine global satellite measurements, at fixed local solar times, are necessary in order that spatial and temporal changes in information can be ascertained and in order to

obtain more conveniently accounts of solar absorption. More information is needed on the anisotropic nature of reflected solar radiation, especially from clouds, on the spectral reflectances and spectral emissivities of terrain and cloud surfaces, and on the significance of aerosol absorption.

Appendix

INFRARED MODEL

The generalized infrared flux model for computing upward and downward fluxes at reference level, R, is described for a single spectral interval by:

$$R > L : F_R\uparrow = B_R - \int_{B_L}^{B_R} \tau_{x,R} dB_x - \beta \left[\int_{B_S}^{B_L} \tau_{x,R} dB + \tau_{s,R} D_s \right]$$

$$- \rho_L \tau_{L,R} \left[\epsilon B_H \tau_{L,H} - \int_{B_L}^{B_H} \tau_{L,y} dB_y \right]$$

$$F_R\downarrow = B_R - \epsilon B_H \tau_{R,H} + \int_{B_R}^{B_H} \tau_{R,y} dB_y,$$

$$R \leq L : F_R\uparrow = B_R - \int_{B_S}^{B_R} \tau_{x,R} dB_y - \tau_{S,R} D_S$$

$$F_R\downarrow = B_R + \int_{B_R}^{B_L} \tau_{R,y} dB_y - \beta \left[\epsilon B_H \tau_{R,H} - \int_{B_L}^{B_H} \tau_{R,y} dB_y \right]$$

$$- \rho_L \tau_{R,L} \left[\int_{B_S}^{B_L} \tau_{x,L} dB_x + \tau_{S,L} D_S \right],$$

where

$$D_S = \rho_S \left[\epsilon\beta B_H \tau_{S,H} - \int_{B_S}^{B_L} \tau_{S,y} dB_y - \beta \int_{B_L}^{B_H} \tau_{S,y} dB_y + \rho_L \tau_{S,L} \int_{B_S}^{B_H} \tau_{x,L} dB_x \right].$$

Subscripts refer to data levels, the symbol τ is the transmission between subscripted levels, and B represents the blackbody flux for the temperature at the data level. The factor ϵ equals unity if the upper boundary is at the top of the model atmosphere; ϵ equals zero otherwise. Other symbols include the reflectance, ρ, at the subscripted level, the transmittance, β, of any semitransparent layer at level L, the upper boundary, H, and the lower boundary, S. Pressure, temperature, and specific humidity at any number of data levels, N, are provided as input data along with the desired initial and final wave numbers and all desired sets of the parameters ρ, β, L, S, H, and R for each computation. In addition, desired view angles are indicated by specifying the cosine of each view angle (0.0 is used to indicate integration over all angles). If no semitransparent level is desired, L can be set equal to a lower or upper boundary and β can be set either to unity or zero. Whenever β is set equal to unity, ρ_L must be given as zero. Parameters required for the transmission computations are loaded with the program.

REFERENCES

1. P. A. Davis, "TIROS III Radiation Measurements and Some Diabatic Properties of the Atmosphere," Mon. Wea. Rev., 93, pp. 535-545 (1965).

2. P. A. Davis and R. L. Mancuso, "TIROS Radiation Measurements and Variations in Atmospheric Heating," Quarterly Progress Report 2, Contract NAS 5-9540, SRI Project 5361, Stanford Research Institute, Menlo Park, California (August 1965).

3. P. A. Davis, "The Application of Infrared Flux Models to Atmospheric Data," J. Appl. Meteor., 4, pp. 263-271 (1965).

4. E. M. Feigelson, M. S. Malkevich, S. Ya. Kogan, T. D. Koronatova, K. S. Glazova, and M. A. Kuznetsova, Calculation of the Brightness of Light in the Case of Anisotropic Scattering (Part 1), Translation, Consultants Bureau, New York (1960).

5. V. S. Atroshenko, E. M. Feigelson, K. S. Glazova, and M. S. Malkevich, Calculation of the Brightness of Light in the Case of Anisotropic Scattering (Part 2), Translation, Consultants Bureau, New York (1963).

6. Ye. M. Feygel'son, Radiation Processes in Stratiform Clouds (Chapter I, Section 5 and Chapter II, Sections 1-7), Translation, Foreign Technology Division, Wright-Patterson Air Force Base, Ohio (1965).

7. C. D. Walshaw, "Integrated Absorption by the 9.6 Micron Band of Ozone," Quart. J. R. Meteor. Soc., 83, pp. 315-321 (1957).

8. W. M. Elsasser, "Atmospheric Radiation Tables," Meteorological Monographs, 4, No. 23 (August 1960).

9. W. S. Hering, "Ozonesonde Observations Over North America," Meteorology Laboratory Project 8631, Office of Aerospace Research, Air Force Cambridge Research Laboratories, L. G. Hanscom Field, Massachusetts (Vol. 1, January 1964; Vol. 2, July 1964).

10. D. Q. Wark, G. Yamamoto, and J. H. Lienesch, "Methods of Estimating Infrared Flux and Surface Temperatures from Meteorological Satellites," J. Atmos. Sci., 19, pp. 369-384 (1962).

11. W. R. Bandeen, M. Halev, and I. Strange, "A Radiation Climatology in the Visible and Infrared from the TIROS Meteorological Satellites," Symposium on Atmospheric Radiation, International Association of Meteorology and Atmospheric Physics (IUGG), Leningrad, U.S.S.R. (August 1964).

12. H. V. Sverdrup, M. W. Johnson, and R. H. Fleming, The Oceans, Prentice-Hall, Inc., Englewood Cliffs, New Jersey (1942).

13. P. A. Davis and W. Viezee, "TIROS Radiation Measurements and Variations in Atmospheric Heating," Quarterly Progress Report 3, Contract NAS 5-9540, SRI Project 5361, Stanford Research Institute, Menlo Park, California (December 1965).

14. R. J. Murgatroyd, "Winds and Temperatures Between 20 km and 100 km - a Review," Quart. J. R. Meteor. Soc., 83, pp. 417-458 (1957).

15. Staff, Goddard Space Flight Center, "TIROS VII Radiation Data Catalog and User's Manual," NASA Goddard Space Flight Center, Greenbelt, Maryland (Vol. 1, September 1964; Vol. 2, December 1964; Vol. 3, October 1965).

NASA-Langley, 1966 CR-581

"The aeronautical and space activities of the United States shall be conducted so as to contribute . . . to the expansion of human knowledge of phenomena in the atmosphere and space. The Administration shall provide for the widest practicable and appropriate dissemination of information concerning its activities and the results thereof."

—NATIONAL AERONAUTICS AND SPACE ACT OF 1958

NASA SCIENTIFIC AND TECHNICAL PUBLICATIONS

TECHNICAL REPORTS: Scientific and technical information considered important, complete, and a lasting contribution to existing knowledge.

TECHNICAL NOTES: Information less broad in scope but nevertheless of importance as a contribution to existing knowledge.

TECHNICAL MEMORANDUMS: Information receiving limited distribution because of preliminary data, security classification, or other reasons.

CONTRACTOR REPORTS: Technical information generated in connection with a NASA contract or grant and released under NASA auspices.

TECHNICAL TRANSLATIONS: Information published in a foreign language considered to merit NASA distribution in English.

TECHNICAL REPRINTS: Information derived from NASA activities and initially published in the form of journal articles.

SPECIAL PUBLICATIONS: Information derived from or of value to NASA activities but not necessarily reporting the results of individual NASA-programmed scientific efforts. Publications include conference proceedings, monographs, data compilations, handbooks, sourcebooks, and special bibliographies.

Details on the availability of these publications may be obtained from:

SCIENTIFIC AND TECHNICAL INFORMATION DIVISION

NATIONAL AERONAUTICS AND SPACE ADMINISTRATION

Washington, D.C. 20546